

# Superposition of Multi-Valued Solutions in High Frequency Wave Dynamics

Hailiang Liu · Zhongming Wang

Received: 3 February 2007 / Accepted: 13 February 2008 / Published online: 11 March 2008  
© Springer Science+Business Media, LLC 2008

**Abstract** The weakly coupled WKB system captures high frequency wave dynamics in many applications. For such a system a level set method framework has been recently developed to compute multi-valued solutions to the Hamilton-Jacobi equation and evaluate position density accordingly. In this paper we propose two approaches for computing multi-valued quantities related to density, momentum as well as energy. Within this level set framework we show that physical observables evaluated in Jin et al. (J. Comput. Phys. 210(2):497–518, 2005; J. Comput. Phys. 205(1):222–241, 2005) are simply the superposition of their multi-valued correspondents. A series of numerical tests is performed to compute multi-valued quantities and validate the established superposition properties.

**Keywords** Level set method · WKB system · Multi-valued solution · Superposition

## 1 Introduction

We consider the WKB system of the form

$$\partial_t S + H(x, \nabla_x S) = 0, \quad t \in \mathbb{R}^+, \quad x \in \mathbb{R}^n, \quad (1.1)$$

$$\partial_t \rho + \nabla_x \cdot (\rho \nabla_p H(x, \nabla_x S)) = 0, \quad p = \nabla_x S \in \mathbb{R}^n, \quad (1.2)$$

subject to the initial data

$$S(0, x) = S_0(x), \quad (1.3)$$

$$\rho(0, x) = \rho_0(x). \quad (1.4)$$

Here  $H(x, p)$  is called Hamiltonian,  $S$  denotes phase and  $\rho$  is position density. This nonlinear system arises in many contexts such as semi-classical approximations of the Schrödinger

---

H. Liu (✉) · Z. Wang  
Mathematics Department, Iowa State University, Ames, IA 50011, USA  
e-mail: [hliu@iastate.edu](mailto:hliu@iastate.edu)

equation

$$i\epsilon \partial_t \psi + \frac{\epsilon^2}{2} \Delta_x \psi = V(x)\psi, \tag{1.5}$$

and high frequency approximations of wave dynamics for hyperbolic equations such as

$$\partial_{tt} u - c^2(x) \Delta_x u = 0. \tag{1.6}$$

The main computational challenge for high frequency wave propagation problems is that the wave field is highly oscillatory, making direct simulation unrealistic. The WKB approximation is a classical way to approximate the wave field through an effective phase and a position density. The WKB system (1.1), (1.2) is formally derived from applying the following ansatz

$$A(t, x) \exp\left(\frac{iS(t, x)}{\epsilon}\right), \tag{1.7}$$

to the original wave equation, see e.g. [32]. The system (1.1) and (1.2) is weakly coupled, thus the effective phase  $S$  can be solved from the Hamilton-Jacobi equation, independent of the density. However, the nonlinearity of the Hamiltonian often leads to kinks in phase at finite time, which forces unbounded density to appear. The classical viscosity solutions [5, 18] are not adequate in describing the wave behavior beyond singularity, where multi-valued solutions in physical space should be considered.

Computation of multi-valued solutions is challenging, there has appeared a bulk of numerical methods to address the difficulty, ranging from Lagrangian methods, Hamilton-Jacobi equation based methods to kinetic formulation based methods. We refer to [7] for a seminal survey on computational high-frequency wave propagation. Recently, a new level set method framework has been developed for computing multi-valued phases and other physical observables in the entire physical domain in [4, 15–17, 19]; main development has been summarized in the review article [20]. A key idea is to represent the  $n$ -dimensional bi-characteristic manifold of the Hamilton-Jacobi equation in phase space by an implicit vector level set function  $\Phi(t, x, p)$ , whose components solve the same Liouville equation

$$\partial_t \Phi + \nabla_p H \cdot \nabla_x \Phi - \nabla_x H \cdot \nabla_p \Phi = 0, \quad \Phi_0 = p - \nabla_x S_0.$$

The multi-valued velocity  $\{u_i(x, t)\}$  is determined by the zero level set, i.e.,

$$u_i(t, x) \in \{p, \Phi(t, x, p) = 0\}, \quad (t, x) \in \mathbb{R}^+ \times \mathbb{R}.$$

The amplitude is hence evaluated by

$$\bar{\rho} = \int f \delta(\Phi) dp,$$

where the quantity  $f$  also solves the same Liouville equation with  $\rho_0$  as initial data. Such a level set method is simple to implement, and in high dimensions more robust than the moment methods [2, 6, 9, 14]. Also the computational cost in the phase space can be reduced by using the local level set method [23, 24, 26]. Recently, an efficient semi-Lagrangian method is introduced in [3] for the phase space wavefront reconstruction in three space dimensions.

Recently a field space based level set method is developed in [21, 22] for computing multi-valued velocity and electric fields governed by 1D Euler-Poisson equations

$$\begin{aligned} \partial_t \rho + \partial_x(\rho u) &= 0, \quad x \in \mathbb{R}, t > 0, \\ \partial_t u + u \partial_x u &= K E, \\ E_x &= \rho - c(x). \end{aligned}$$

In particular, multi-valued density is computed from

$$\rho_i \in \left\{ \frac{f}{\left| \det \left( \frac{\partial(\phi_1, \phi_2)}{\partial(p, q)} \right) \right|} \Big| \phi_1 = 0, \phi_2 = 0 \right\},$$

where  $\phi_1, \phi_2$  are two level set functions satisfying the transport equation,

$$\Phi_t + p \Phi_x + K q \Phi_p - c(x) p \Phi_q = 0, \quad \Phi = [\phi_1, \phi_2]^T$$

and  $f$  solves the same transport equation in field space  $(x, p, q)$ , subject to the given initial density  $\rho_0$ . It was shown that a superposition of these multi-valued density gives the averaged density over the zero level set manifold. Note that the obtained density from this formula will become unbounded wherever  $\frac{\partial(\phi_1, \phi_2)}{\partial(p, q)}$  becomes zero, which corresponds to the density concentration near focus of particle paths. This phenomenon is verified by the sharp peaks in numerical examples.

The aim of this paper is to compute multi-valued quantities related to density, momentum and energy, and conduct numerical comparison with the averaged physical observables evaluated in [15, 16]. Following [22], we shall compute multi-valued density of the WKB system (1.1)–(1.2) either by

$$\rho_i \in \left\{ \frac{f}{\left| \det(\nabla_p \Phi) \right|} \Big| \Phi(t, x, p) = 0 \right\}, \tag{1.8}$$

or

$$\rho_i \in \left\{ \frac{\rho_0(\alpha)}{\left| \det \left( \frac{\partial x(t, \alpha)}{\partial \alpha} \right) \right|} \Big| x = x(t, \alpha) \right\}, \tag{1.9}$$

where  $x(t, \alpha)$  denotes the deformation map satisfying  $\frac{dx}{dt} = \nabla_p H(x, p)|_{p=\nabla_x S}$  with  $x(t, 0) = \alpha$ . As remarked above, these two formulas are valid both before and after the caustics.

Within the level set framework we prove that the averaged density  $\bar{\rho}$  is simply a linear superposition of multi-valued density, i.e.,

$$\bar{\rho}(t, x) = \sum_{i=1}^N \rho_i(t, x),$$

where  $\rho_i$  is the  $i^{th}$  branch of multi-valued density ( $1 \leq i \leq N$ ). Similar superposition properties are shown to also hold for other quantities such as momentum and energy. These properties are confirmed by a series of numerical examples.

We now conclude this section by outlining the rest of this paper. In Sect. 2 we review the level set framework introduced in [4, 16, 17], to compute multi-valued velocity, phase and

averaged density of the system (1.1) and (1.2), since our results are based on the formulation derived therein. In Sect. 3 we discuss two techniques for computing the multi-valued density, one by the level set method, and another by the Lagrangian method. Superposition properties for multi-valued density, momentum as well as energy are established in Sect. 4. Numerical procedures are detailed in Sect. 5. Finally, in Sect. 6 a series of numerical examples is presented to compute multi-valued observables and validate the superposition properties. Justification of the formula (1.9) is given in the Appendix.

## 2 Review of Level Set Formulation and Computation of Averaged Density

### 2.1 Level Set Formulation for Velocity

The classical way to compute the multi-valued solution is to use Lagrangian method, i.e., following the characteristics of the Hamilton-Jacobi equation (1.1),

$$\frac{dx}{dt} = \nabla_p H(x, p), \quad \frac{dp}{dt} = -\nabla_x H(x, p), \tag{2.1}$$

$$x(0) = \alpha, \quad p(0) = \nabla_x S_0(\alpha). \tag{2.2}$$

Here  $p$  is the moment variable in phase space, i.e.,  $p = \nabla_x S$ .

Following [4], let  $\Phi(t, x, p)$  be a global invariant of (2.1) in the  $(x, p)$  space, then

$$\frac{d}{dt} \Phi(t, x(t), p(t)) \equiv 0,$$

which leads to the following level set equation

$$\partial_t \Phi + \nabla_p H(x, p) \cdot \nabla_x \Phi - \nabla_x H(x, p) \cdot \nabla_p \Phi = 0. \tag{2.3}$$

Thus the multi-valued velocity is determined by the zero level set of  $\Phi$ . The initial condition could be chosen as

$$\Phi(0, x, p) = p - \nabla_x S_0(x). \tag{2.4}$$

Note that other choice of initial data is also admissible, as long as its zero level set uniquely determines the initial phase gradient  $\nabla_x S_0$ . We will see in later sections that the choice (2.4) would simplify the post processing in the evaluation of density  $\rho$ .

### 2.2 Level Set Formulation for both Velocity and Phase

In addition to the bi-characteristic system (2.1), we have

$$\frac{dS(t, x)}{dt} = -H(x, p) + p \cdot \nabla_p H(x, p), \quad S(0, x) = S_0(\alpha). \tag{2.5}$$

Similarly let  $\Phi(t, x, p, q)$  be a global invariant in the  $(x, p, q)$  space with  $q = S$  along the zero level set, then

$$\frac{d}{dt} \Phi(t, x(t), p(t), q(t)) \equiv 0,$$

which becomes

$$\partial_t \Phi + \nabla_p H \cdot \nabla_x \Phi - \nabla_x H \cdot \nabla_p \Phi + (p \cdot \nabla_p H - H) \partial_q \Phi = 0. \tag{2.6}$$

The initial condition for  $\Phi = (\phi_1, \phi_2, \dots, \phi_{n+1})^T$  could be chosen as

$$\begin{aligned} \phi_i(0, x, p, q) &= p_i - \partial_{x_i} S_0(x), \quad i = 1, 2, \dots, n \\ \phi_{n+1}(0, x, p, q) &= q - S_0(x). \end{aligned}$$

Here the necessity of doing computation in  $2n + 1$ -dimension space is to capture the phase  $S$  as well. However, as pointed out in [4], multi-valued phase can also be recovered in phase space by

$$S(t, x) \in \{ \tilde{S}(t, x, p) \mid \Phi(t, x, p) = 0 \},$$

where the level set function  $\Phi$  is solved from (2.3), and  $\tilde{S}$  solves

$$\begin{aligned} \partial_t \tilde{S} + \nabla_p H \cdot \nabla_x \tilde{S} - \nabla_x H \cdot \nabla_p \tilde{S} &= p \cdot \nabla_p H - H, \\ \tilde{S}(0, x, p) &= S_0(x). \end{aligned}$$

### 2.3 Evaluation of Averaged Density

Let  $f$  be a function solving

$$f_t + \nabla_p H \cdot \nabla_x f - \nabla_x H \cdot \nabla_p f = 0, \quad f_0 = \rho_0. \tag{2.7}$$

Then the average density can be determined by

$$\bar{\rho}(t, x) = \int_{\mathbb{R}^n} f \delta(\Phi) dp. \tag{2.8}$$

Note that the momentum  $\bar{J}$  and energy  $\bar{E}$  can be evaluated by

$$\bar{J} = \int_{\mathbb{R}^n} H_p(x, p) f \delta(\Phi) dp, \tag{2.9}$$

$$\bar{E} = \int_{\mathbb{R}^n} H(x, p) f \delta(\Phi) dp. \tag{2.10}$$

### 3 Computation of Multi-Valued Density

As is known, the position density, say  $|\Psi^\epsilon|^2$  for (1.5), also becomes oscillatory as  $\epsilon \rightarrow 0$ . The quantity computed in (2.8) may be regarded as the weak limit of the position density. We now show how to compute the multi-valued density to the WKB system through this level set approach.

Let  $L$  be a Liouville operator given by

$$L := \partial_t + \nabla_p H \cdot \nabla_x - \nabla_x H \cdot \nabla_p,$$

and  $\tilde{\rho}$  be a representation of  $\rho(t, x)$  in phase space with  $\tilde{\rho}(t, x, \nabla_x S) = \rho(t, x)$  and  $J = \det(\nabla_p \Phi)$ , then it is shown in [16] that

$$L(\tilde{\rho}|J) \equiv 0. \tag{3.1}$$

The equation (2.7) can be rewritten as

$$L(f) = 0, \quad f_0 = \rho_0. \tag{3.2}$$

This shows that  $f$  and  $\tilde{\rho}|J|$  satisfies the same Liouville equation with the same initial condition ( $|J_0| = 1$ ). Therefore, after we solve (2.3) for  $\Phi$  and (2.7) for  $f$ , uniqueness leads to

$$f = \tilde{\rho}|J|. \tag{3.3}$$

Hence, we can determine multi-valued density by

$$\rho_i \in \left\{ \frac{f}{|\det(\nabla_p \Phi)|} \mid \Phi(t, x, p) = 0 \right\}. \tag{3.4}$$

Note that the formula (3.4) remains valid wherever  $|\det(\nabla_p \Phi)| \neq 0$ .

We now summarize the procedure for computation of the multi-valued density in general setting using the following pseudo-algorithm:

1. Solve the level set equation (2.3) for  $\Phi$  and (2.7) for  $f$ .
2. Compute  $|\det(\nabla_p \Phi)|$ . It is simple to evaluate the determinant for  $n = 1, 2, 3$ .
3. Evaluate the quantity  $\frac{f}{|\det(\nabla_p \Phi)|}$  on zero level set of  $\Phi$ .

The above approach works in all settings and it is sometimes possible to adopt an easier approach in specific cases.

Recalling the ODE system (2.1), if we can solve  $x$  and  $p$  in terms of  $t$  and  $\alpha$  explicitly, we could use Lagrangian approach to evaluate multi-valued density. By defining

$$\Gamma(t, \alpha) = \nabla_\alpha x, \tag{3.5}$$

we can find density by the following parameterized solution

$$\rho(t, x(t, \alpha)) = \frac{\rho_0(\alpha)}{|\det(\Gamma)|}. \tag{3.6}$$

The justification of this formula is given in the Appendix of this paper.

### 4 Superposition

In this section we show that the linear superposition principle holds for the density of the general WKB system (1.1) and (1.2) in the sense that direct summation of all multi-valued densities gives the physical observed density, i.e.,

$$\tilde{\rho}(t, x) = \sum_{i=1}^N \rho_i(t, x). \tag{4.1}$$

This superposition actually also holds for other physical observables, as summarized below.

**Theorem 4.1** (Superposition Principle for General Function  $g(x, p)$ ) *Let  $\{\rho_i\}_{i=1}^N$  be multi-valued densities corresponding to multi-valued fields  $u_i$  determined by*

$$u_i \in \{p \mid \Phi(t, x, p) = 0\},$$

and  $g(x, p)$  be any smooth function of  $x$  and  $p$ . Let

$$G = \int fg\delta(\Phi)dp,$$

where  $f$  solves (2.7) and  $\Phi$  solves (2.3) with initial condition (2.4). Then

$$G = \sum_{i=1}^N g(x, u_i)\rho_i(t, x). \tag{4.2}$$

*Proof* First note that here  $u_i$  denotes  $i^{th}$  branch of multi-valued  $u$  instead of  $i^{th}$  component of vector  $u$ . In order to evaluate the integral for  $G$ , we assume that all  $(u_i$ 's) lie in a bounded domain. Use a partition of unity,  $\sigma_i \in C_0^\infty$ , non-vanishing near  $u_i$ , with  $\sigma_i(u_i) = 1$  and  $\sum \sigma_i = 1$ , we have

$$\int_{\mathbb{R}^n} fg\delta(\Phi)dp = \sum_{i=1}^N \int_{\mathbb{R}^n} fg\sigma_i\delta(\Phi)dp.$$

It suffices to evaluate  $\int fg\sigma_i\delta(\Phi)dp$ .

Recall that

$$\delta(\Phi(t, x, p)) = \sum_{k=1}^N \frac{\delta(p - u_k)}{|\nabla_p \Phi(t, x, u_k)|},$$

wherever  $|\nabla_p \Phi(t, x, u_k)|$  is nonzero.

At  $p = u_i$ , (3.3) gives

$$f(t, x, u_i) = \tilde{\rho}(t, x, u_i)|J|. \tag{4.3}$$

Thus near each  $u_i$ -support( $\sigma_i$ ), we have

$$\begin{aligned} \int_{\mathbb{R}^n} \sigma_i fg\delta(\Phi)dp &= \int_{\mathbb{R}^n} \sigma_i \tilde{\rho}|J|g \sum_{k=1}^N \frac{\delta(p - u_k)}{|J|} dp \\ &= \int_{\text{support}(\sigma_i)} \tilde{\rho}|J|g \frac{\delta(p - u_i)}{|J|} dp \\ &= \tilde{\rho}(t, x, u_i)g(t, x, u_i) \\ &= \rho_i(t, x)g(t, x, u_i). \end{aligned}$$

This, combined with the partition of unity, gives the asserted (4.2). □

### 5 Numerical Implementation

In this section, we summarize our numerical procedures to compute the multi-valued velocity and other quantities. We also verify the superposition property stated in Theorem 4.1.

**Step 1.** Discretization and Initialization

We will use uniform mesh size  $(\Delta x, \Delta p)$  in  $x$  and  $p$ . The computation domain is determined by using bi-characteristics if possible. The guideline is that the domain should cover the range of velocity in  $p$  direction and contain at least one period of initial velocity in  $x$  for periodic initial data. In practice we choose periodic boundary condition in the simulation.

**Step 2.** Solve the level set equation (2.3) for  $\Phi$  and (2.7) for  $f$ .

In 1D case, the transport equation (2.3) and (2.7) is semi-discretized as

$$\frac{d\Phi^{ij}(t)}{dt} = -H_p^{ij}(t)\Phi_x^{ij}(t) + H_x^{ij}(t)\Phi_p^{ij}(t) := \mathcal{P}(\Phi^{ij}(t)),$$

where  $H^{ij}(t)$  and  $\Phi^{ij}(t)$  is the numerical approximation of  $H$  and  $\Phi$  at node  $(x_i, p_j)$ . Usually,  $H_p$  and  $H_x$  are given explicitly and  $\Phi_x, \Phi_p$  can be approximated by  $r^{th}$  order ENO scheme [12, 13, 25, 28, 30]. In our simulation, second order ENO approximation is applied.

Then, for time discretization we use second order Runge-Kutta method,

$$\begin{aligned} k^{ij} &= \Phi^{ij}(t) + \Delta t \mathcal{P}(\Phi^{ij}(t)), \\ \Phi^{ij}(t + \Delta t) &= \frac{1}{2} \Phi^{ij}(t) + \frac{1}{2} (k^{ij} + \Delta t \mathcal{P}(k^{ij})). \end{aligned} \tag{5.1}$$

This method is also known as Heun’s method, which has been implemented in [29]. However, we refer it as second order Runge-Kutta method, which can be easily extended to higher order schemes in the category of SSP Runge-Kutta method, see in [11].

**Step 3.** Visualize the multi-valued velocity by plotting the zero level set of  $\Phi$  in  $(x, p)$  space.

In 1D case, for the velocity, we plot out only grid points satisfying

$$\{(x_i, p_j) \in \Omega \mid |\Phi(t, x_i, p_j)| < \epsilon'\},$$

where  $\epsilon'$  is chosen in such a way that a unique grid point can be identified along the zero level set. Since it is computationally impossible to find the points where  $\Phi$  is exactly zero, the zero level set of  $\Phi$  is realized within a small interval of zero, i.e., any points, with function value close enough to zero, will be considered in the zero level set. We point out that a larger  $\epsilon'$  may be necessary for the case when level set functions are rough.

**Step 4.** Evaluate the integral (2.8)

$$\bar{\rho}^{int}(t, x) = \int_{\mathbb{R}} f \delta(\Phi) dp.$$

Since this integration involves the Dirac  $\delta$ -function in its integrand, as usual we first regularize the Dirac  $\delta$ -function by a smooth bounded function  $\delta_\epsilon$  in such a way that  $\delta_\epsilon \rightarrow \delta$  as  $\epsilon \rightarrow 0^+$ . The error introduced in this regularization step depends on the choice of the approximation, whose accuracy is indicated by a so called moment condition [1] of the regularization.  $\delta_\epsilon$  is said to satisfy  $r^{th}$  order of moment condition if  $\int_{\mathbb{R}} \delta_\epsilon(x) dx = 1$  and  $\int_{\mathbb{R}} \delta_\epsilon(x) x^k dx = 0$  for  $1 \leq k \leq r$ . Under the condition that  $\delta_\epsilon$  is sufficiently resolved by the

grid, it is known that the higher the order of moment condition, the smaller the regularization error. Otherwise, the concept of discrete moments should be introduced, see e.g. [8]. The choice of regularization  $\delta_\epsilon$  could be any smooth function with the above properties. However, considering the concentration of the  $\delta$ -function, it suffices to choose  $\delta_\epsilon$  to have a compact support:

$$\delta_\epsilon(x) = \begin{cases} \frac{1}{\epsilon} \Psi\left(\frac{x}{\epsilon}\right), & |x| \leq \epsilon, \\ 0, & |x| > \epsilon. \end{cases}$$

One of the well accepted choices of this type of  $\delta_\epsilon$  is the cosine kernel,  $\Psi(\eta) = \frac{1}{2}(1 + \cos(\pi\eta))$ , i.e.,

$$\delta_\epsilon^{\text{cos}}(x) = \frac{1}{2\epsilon} \left(1 + \cos\left(\frac{\pi x}{\epsilon}\right)\right) I_{[-\epsilon, \epsilon]}, \tag{5.2}$$

which has first order moment condition. Here  $I_{[-\epsilon, \epsilon]}$  is the standard indicator function.

Replacing  $\delta(\Phi)$  by  $\delta_\epsilon(\Phi)$ , we thus have the first approximation of  $\bar{\rho}$ ,

$$\bar{\rho}_\epsilon^{\text{int}}(t, x) = \int_{\mathbb{R}} f(t, x, p, ) \delta_\epsilon(\Phi) dp, \tag{5.3}$$

to which standard quadrature rules can be applied. In our simulation, the rectangle rule is chosen and the numerical density is further evaluated by

$$\bar{\rho}_{\epsilon h}^{\text{int}}(t, x) = \sum_{\{|\Phi(t, x, p_j)| \leq \epsilon\}} f(t, x, p_j) \delta_\epsilon^{\text{cos}}(\Phi) \Delta p. \tag{5.4}$$

In this two-step procedure, total error is bounded by the sum of regularization error  $|\bar{\rho}^{\text{int}} - \bar{\rho}_\epsilon^{\text{int}}|$  and quadrature error  $|\bar{\rho}_\epsilon^{\text{int}} - \bar{\rho}_{\epsilon h}^{\text{int}}|$ . For example, if the cosine kernel and the rectangle rule are used,  $|\bar{\rho}^{\text{int}} - \bar{\rho}_\epsilon^{\text{int}}|$  is of order  $\epsilon$  and  $|\bar{\rho}_\epsilon^{\text{int}} - \bar{\rho}_{\epsilon h}^{\text{int}}|$  is of order  $h/\epsilon$ , where  $h = \Delta p$ . Then the optimal  $\epsilon$  would be order of  $\sqrt{h}$ , which leads to order of  $\sqrt{h}$  in total error. In the simulation,  $\epsilon$  is tested with a range of quantities proportional to  $h$ , i.e.,  $\epsilon = mh$ ,  $m = 1, 2, \dots$ . See [8, 22, 27, 31] for details on the error analysis of approximating  $\delta$ -functions. Keeping a constant ratio between  $h$  and  $\epsilon$  may lead to inconvergence, as pointed out in [8].

**Step 5.** Computation of multi-valued density  $\{\rho_i\}$ .

We compute the multi-valued density by (3.4) and the detailed algorithm is discussed in Sect. 3 for the WKB system (2.1)–(2.2) with general Hamiltonian. However, in cases where  $\Gamma = \nabla_\alpha x(t, \alpha)$  can be explicitly expressed in terms of  $\alpha$  and  $t$ , we choose to use formula (3.6), i.e.,

$$\rho(t, x(t, \alpha)) = \frac{\rho_0(\alpha)}{|\det(\Gamma)|}.$$

This formula gives a parameterized solution in terms of  $\alpha$  and thus can be used to plot the contour of  $\rho$  in  $(x, \rho)$  space. In simulation, we first discretize  $\alpha$  into nodes  $\{\alpha_k | k = 1, 2, \dots\}$  and compute  $(x(t, \alpha_k), \rho(t, x(t, \alpha_k)))$ . Then linear interpolation is used locally for any points wherever function values are needed. In this manner,  $\rho(t, x)$  can be evaluated at any point  $x_i$ . Note that, in our simulation we will utilize this formula (3.6) to compute exact multi-valued solution whenever  $\Gamma$  is available.

**Step 6.** Verify the superposition by comparing  $\bar{\rho}_{\epsilon h}^{\text{int}}$  and  $\bar{\rho} := \sum_i^N \rho_i$  using both figures and tables of  $L^1$  errors. In one dimension with uniform mesh size in  $x$ , the  $L^1$  error for  $\bar{\rho}$  is

defined by

$$Error_{\bar{\rho}} = \sum_i |\rho_{eh}^{int}(t, x_i) - \bar{\rho}(t, x_i)| \Delta x,$$

where  $\rho_{eh}^{int}(t, x_i)$  and  $\bar{\rho}(t, x_i)$  are defined by (4.1) and (5.4). Similar definitions apply to other quantities of interest.

## 6 Numerical Examples

### 6.1 The Schrödinger Equation

In this section, the Hamiltonian is of the form

$$H(x, p) = \frac{1}{2}|p|^2 + V,$$

which arises in the semi-classical approximation of the Schrödinger equation (1.5).

We are interested in density  $\bar{\rho}$ , the momentum  $\bar{J}$  and energy  $\bar{E}$ , where

$$\begin{aligned} \bar{\rho} &= \int f \delta(\Phi) dp, \\ \bar{J} &= \int |p| f \delta(\Phi) dp, \\ \bar{E} &= \int \left( \frac{1}{2}|p|^2 + V \right) f \delta(\Phi) dp. \end{aligned}$$

We make numerical comparison of the averaged quantities computed from two approaches, integration or superposition. Note here that in order to use superposition, we have two ways to prepare the multi-valued density, which includes (3.6) and (3.4). Equation (3.6) is used whenever the ODE system (2.1) can be solved explicitly.

*Example 1* 1D and  $V = 0$

$$\begin{aligned} u_0 &= -\sin(\pi x), \\ \rho_0 &= \exp(-(x - 0.5)^2). \end{aligned}$$

This example was used in [10]. Throughout the numerical simulation, unless otherwise specified, second order ENO and second order SSP Runge-Kutta methods are used. The CFL number is taken to be 0.95 to ensure the time efficiency. In what follows, for the density, circles denote the numerical results computed from (5.4), and this is further noted as results from integration. Solid lines represent the results from either ODE system (3.6) and superposition (4.1), whenever the ODE system can be solved explicitly, or level set method (2.7), multi-valued density (3.4) and superposition (4.1). This is further referred as results from superposition. Similar notation are used for the representation of other quantities as well. In this simulation, computational domain is  $[-1, 1] \times [-1.5, 1.5]$  with step sizes (0.02, 0.02) and time at about 0.1, 0.3 and 0.6. The multi-valued density is computed by (3.6), since the problem is potential free and the exact parametric solution can be written down explicitly.

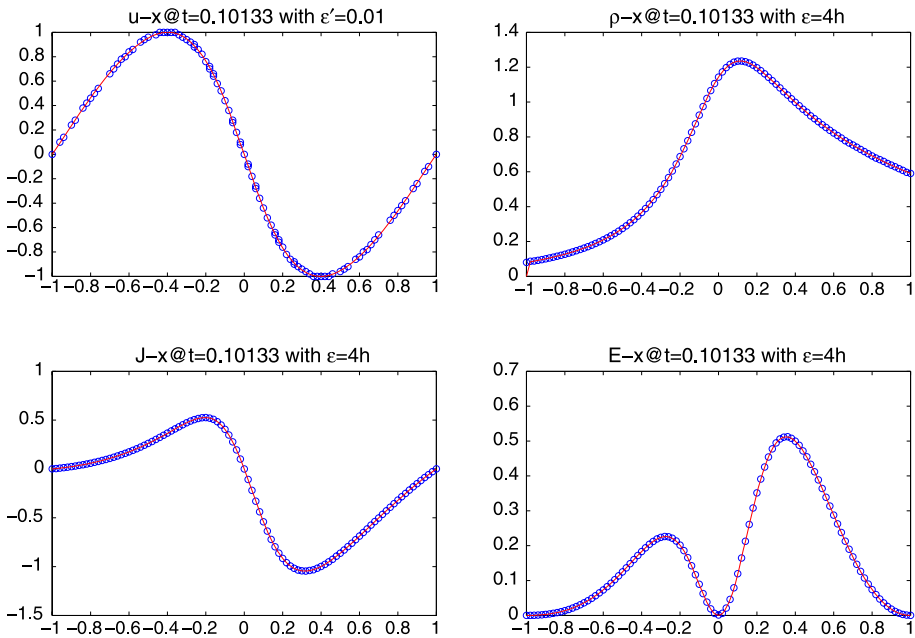


**Fig. 1** Example 1, at  $t = 0.101333$ . Sub-figures, from *up left*, are velocity, density, momentum and energy with  $\epsilon' = 0.01$  and  $\epsilon = 4h$ . Circles and solid lines represent the results from integration and superposition, respectively

Here, periodic and constant boundary conditions are used in computing  $\Phi$  and  $f$ , respectively.

From Figs. 1, 2 and 3, we can clearly see the capacity of our method. Before singularity—when system develops multi-valuedness, two results are the same and after singularity, peaks in all the three quantities are well captured, i.e., the circle goes up when there is a peak in the solid line.

Table 1 shows the  $L^1$  error for the averaged density  $\bar{\rho}$ , momentum  $\bar{J}$  and energy  $\bar{E}$ , which correspond to the quantities defined in Theorem 4.1 with  $g = 1$  and  $g = p$  and  $g = |p|^2/2$  respectively. Moreover, we also notice that there is an optimal  $\epsilon$  as we pick different  $m$  in  $\epsilon = mh$ . At time 0.101333 the errors in  $\bar{\rho}$ ,  $\bar{J}$  and  $\bar{E}$  are of order  $10^{-2}$ ,  $10^{-4}$  and  $10^{-4}$ , respectively, with step sizes  $\Delta x = 0.02$  and  $\Delta p = 0.02$  at the optimal  $\epsilon$ . After singularity we still get very good resolution as seen in Figs. 2 and 3.

We also notice the effect of integration support  $\epsilon$  on the error. Before multi-valued solution appears, the larger the size of the support  $\epsilon$  tends to give better accuracy, due to the smoothness of the solution. We can see this from the errors for the average density, momentum and energy at time 0.101333 in Table 1. In the case under consideration  $\epsilon = mh$  when  $m = 4$  or 5 gives better results in our integration approximation. However, after the formation of multi-valuedness, we have to pick smaller  $\epsilon$ .

We then refine our mesh size to be  $[0.01, 0.01]$ , and similar observation is also made in Table 2. When we further refine the mesh size to be  $[0.005, 0.005]$ , before singularity the error can be seen in Table 3. However, after singularity, we have to use very small integration support say  $1h$ , see in Table 4. The figures are similar to what we obtained by coarse mesh (not presented here).

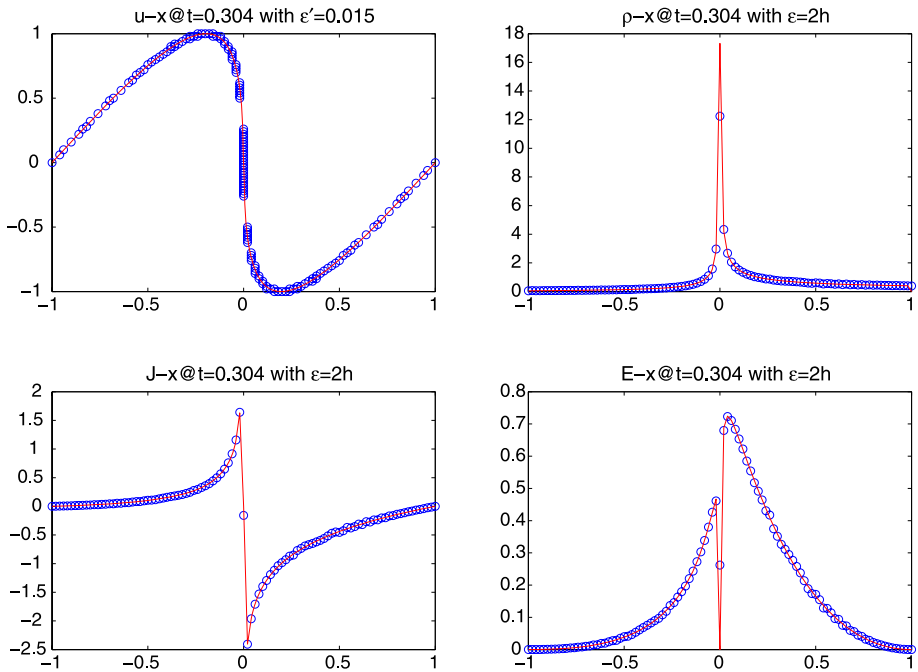


**Fig. 2** Example 1, at  $t = 0.304000$ . Sub-figures, from *up left*, are velocity, density, momentum and energy with  $\epsilon' = 0.015$  and  $\epsilon = 2h$ . Circles and solid lines represent the results from integration and superposition, respectively

**Table 1** Example 1, table of  $L^1$  error for each density, momentum and energy at different time and support size  $\epsilon = mh$ ,  $m = 2, 3, 4, 5, 6$  with mesh size  $[0.02, 0.02]$

1. Error for averaged density  $\bar{\rho}$

$t$	$\epsilon = 2h$	$\epsilon = 3h$	$\epsilon = 4h$	$\epsilon = 5h$	$\epsilon = 6h$
0.101333	0.0167394677	0.0135057820	0.0126285789	0.0123750004	0.0122404699
0.304000	0.1293897319	0.1670558597	0.2117553210	0.2512718005	0.2806063519
0.608000	0.2105845480	0.1407095069	0.1774095427	0.2056773509	0.2268914252

2. Error for averaged momentum  $\bar{J}$

$t$	$\epsilon = 2h$	$\epsilon = 3h$	$\epsilon = 4h$	$\epsilon = 5h$	$\epsilon = 6h$
0.101333	0.0034993097	0.0010479213	0.0005364168	0.0004407054	0.0005107636
0.304000	0.0131135016	0.0098454853	0.0143602091	0.0225903714	0.0328003001
0.608000	0.1406452841	0.1122488771	0.1434971805	0.1673175011	0.1849303384

3. Error for averaged energy  $\bar{E}$

$t$	$\epsilon = 2h$	$\epsilon = 3h$	$\epsilon = 4h$	$\epsilon = 5h$	$\epsilon = 6h$
0.101333	0.0014676255	0.0005905758	0.0006434041	0.0008985308	0.0012774845
0.304000	0.0092880972	0.0102827107	0.0141035968	0.0162260022	0.0177831562
0.608000	0.0570531980	0.0486087232	0.0624852617	0.0724525964	0.0798224902

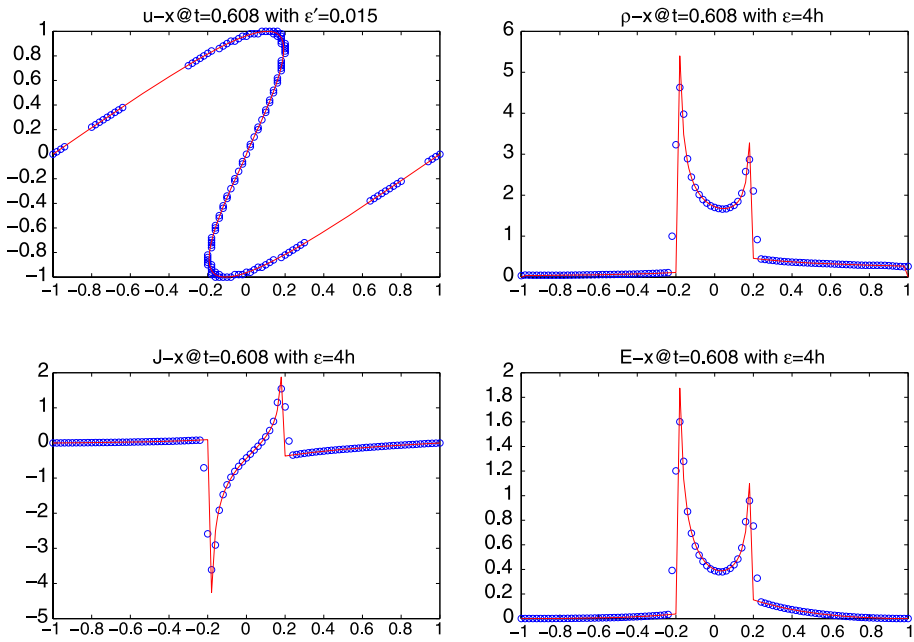


**Fig. 3** Example 1, at  $t = 0.608000$ . Sub-figures, from *up left*, are velocity, density, momentum and energy with  $\epsilon' = 0.015$  and  $\epsilon = 4h$ . *Circles and solid lines* represent the results from integration and superposition, respectively

**Table 2** Example 1, table of  $L^1$  error for each density, momentum and energy at different time and support size  $\epsilon = mh$ ,  $m = 2, 3, 4, 5, 6$  with mesh size  $[0.01, 0.01]$

1. Error for averaged density  $\bar{\rho}$

$t$	$\epsilon = 2h$	$\epsilon = 3h$	$\epsilon = 4h$	$\epsilon = 5h$	$\epsilon = 6h$
0.101333	0.0051376816	0.0017909586	0.0007273995	0.0004612454	0.0002879974
0.304000	0.0401613828	0.0540509632	0.0742904492	0.0939465245	0.1097445398
0.601667	0.1790942828	0.1392930622	0.1715167965	0.2018234660	0.2187257480

2. Error for averaged momentum  $\bar{J}$

$t$	$\epsilon = 2h$	$\epsilon = 3h$	$\epsilon = 4h$	$\epsilon = 5h$	$\epsilon = 6h$
0.101333	0.0037886964	0.0010317342	0.0004580228	0.0002600766	0.0001834229
0.304000	0.0087517411	0.0050335903	0.0062053525	0.0100639636	0.0146909349
0.601667	0.1195325754	0.1245457938	0.1682407453	0.1991976845	0.2142569738

3. Error for averaged energy  $\bar{E}$

$t$	$\epsilon = 2h$	$\epsilon = 3h$	$\epsilon = 4h$	$\epsilon = 5h$	$\epsilon = 6h$
0.101333	0.0015507135	0.0004300757	0.0002650783	0.0002767778	0.0003522299
0.304000	0.0044669558	0.0037550843	0.0044664726	0.0054104155	0.0060948187
0.601667	0.0473188337	0.0605047765	0.0904420081	0.1071774789	0.1139000534

**Table 3** Example 1, table of  $L^1$  error for each density, momentum and energy at different time before singularity and support size  $\epsilon = mh$ ,  $m = 2, 3, 4, 5, 6$  with mesh size [0.005, 0.005]

1. Error for averaged density  $\bar{\rho}$

$t$	$\epsilon = 2h$	$\epsilon = 3h$	$\epsilon = 4h$	$\epsilon = 5h$	$\epsilon = 6h$
0.101333	0.0054255900	0.0019348151	0.0007616662	0.0004350618	0.0002721383
0.300833	0.0186806191	0.0147565168	0.0193886939	0.0388620747	0.0582130475

2. Error for averaged momentum  $\bar{J}$

$t$	$\epsilon = 2h$	$\epsilon = 3h$	$\epsilon = 4h$	$\epsilon = 5h$	$\epsilon = 6h$
0.101333	0.0040379382	0.0011509129	0.0005013195	0.0002428330	0.0001554436
0.300833	0.0144889280	0.0096615926	0.0123598190	0.0361839326	0.0600986628

3. Error for averaged energy  $\bar{E}$

$t$	$\epsilon = 2h$	$\epsilon = 3h$	$\epsilon = 4h$	$\epsilon = 5h$	$\epsilon = 6h$
0.101333	0.0016727121	0.0004593942	0.0002253712	0.0001354775	0.0001186966
0.300833	0.0079236149	0.0057813211	0.0075974680	0.0246010823	0.0414202958

**Table 4** Example 1, table of  $L^1$  error for each density, momentum and energy after singularity at time 0.402167 and support size  $\epsilon = mh$ ,  $m = 1, 1.5, 2, 2.5, 3$  with mesh size [0.005, 0.005]

Quantity	$\epsilon = h$	$\epsilon = 1.5h$	$\epsilon = 2h$	$\epsilon = 2.5h$	$\epsilon = 3h$
$\bar{\rho}$	0.3043520483	0.1102531630	4.2457918328	75.4350338239	137.7567242360
$\bar{J}$	0.1683337070	0.0529774237	6.3482644876	113.1095259437	206.5710968736
$\bar{E}$	0.0584617304	0.0167521244	4.7568178601	84.8200884047	154.9095826285

**Table 5** Example 1, table of  $\min_{|\phi| \leq 0.01} |\phi_p|$  at different times and mesh sizes

$[\Delta x, \Delta p]$	Time $\approx 0.1$	Time $\approx 0.3$	Time $\approx 0.6$
[0.02, 0.02]	0.681654	0.045015	0.328696
[0.01, 0.01]	0.681652	0.044970	0.040079
[0.005, 0.005]	0.681652	0.054908	0.002519*

\*Time at around 0.4

From the integration formula we see that the support  $\epsilon$  of  $\delta(\phi)$  should be chosen in proportional to a product of  $|\phi_p|$  and mesh size in  $p$  direction for each fixed  $x$ . When  $x$  runs over a narrow band of the level set curve  $\{(x, p), \phi(x, p) = 0\}$ , the support  $\epsilon$  is expected to be as

$$\epsilon \sim \min |\nabla_p \phi(x, p)|h, \tag{6.1}$$

which is evidenced by our numerical results described below. In Table 5, we see that  $\min_{|\phi(x,p)| \leq 0.01} |\phi_p|$  becomes smaller when singularity shows up. It tells us that smaller

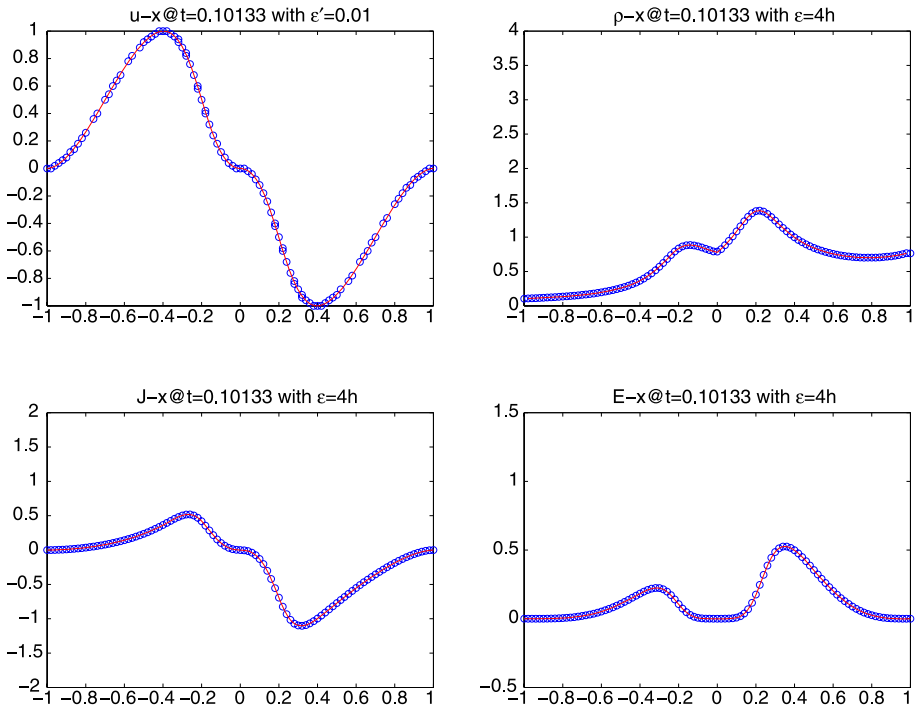


**Fig. 4** Example 2, at  $t = 0.10133$ . Sub-figures, from *up left*, are velocity, density, momentum and energy with  $\epsilon' = 0.01$  and  $\epsilon = 4h$ . Circles and solid lines represent the results from integration and superposition, respectively

$\min_{|\phi| \leq 0.01} |\phi_p|$  results in smaller optimal support size  $\epsilon$ . Especially, at time about 0.4 with mesh size  $[0.05, 0.05]$ ,  $\min_{|\phi| \leq 0.01} |\phi_p|$  becomes very small and hence we must choose small  $\epsilon$ . In this case even  $2h$  will result in big errors as we see in Table 4. Another interesting case is that when mesh size is  $[0.02, 0.02]$ ,  $\min_{|\phi| \leq 0.01} |\phi_p|$ 's are 0.681654, 0.045015 and 0.328696 at time about 0.1, 0.3 and 0.6, respectively. Accordingly the optimal  $\epsilon$ 's in Table 1 are  $6h$ ,  $2h$  and  $3h$  respectively, which confirms that the smaller  $\min_{|\phi| \leq 0.01} |\phi_p|$  is, the smaller optimal  $\epsilon$  is. Similar phenomenon is also observed in other examples. Note that the dependence of optimal support size  $\epsilon$  on  $\phi_p$  has also been studied in [8, 16].

Finally, we make a special remark on the distribution of circles in the multi-valued velocity. In the up-left sub-figures in Figs. 2 and 3, where we observe uneven distributions of circles. This is largely caused by the projection of  $\Phi$  onto its zero level set. Since the zero level set of  $\Phi$  doesn't always go through our computational grid points, we can only pick out those which are very close to grid points. This wiggles in multi-valued velocity can be improved by choosing finer grids.

*Example 2* 1D and  $V = 0$

$$u_0 = -\sin(\pi x) |\sin(\pi x)|,$$

$$\rho_0 = \exp(-(x - 0.5)^2),$$

which was used in [10].

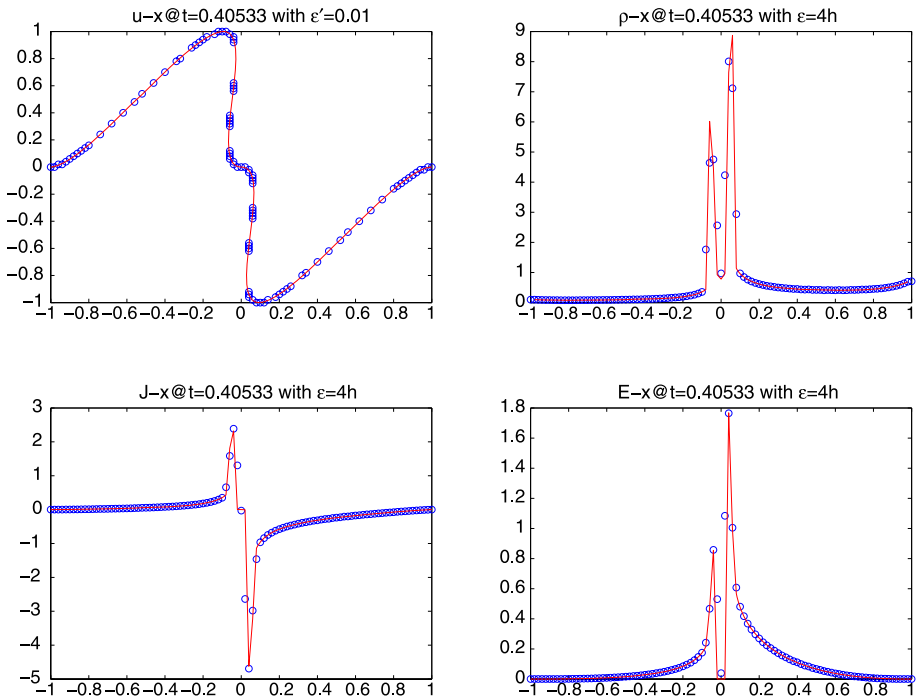


**Fig. 5** Example 2, at  $t = 0.405333$ . Sub-figures, from up left, are velocity, density, momentum and energy with  $\epsilon' = 0.01$  and  $\epsilon = 4h$ . Circles and solid lines represent the results from integration and superposition, respectively

At time about 0.1, 0.4 and 0.8 with step size  $[0.02, 0.02]$  we use second order ENO and second SSP Runge-Kutta method, and the result are plotted in Figs. 4, 5 and 6. In this example, the multi-valued density is computed by (3.6).

In Figs. 4, 5 and 6, we notice that the results from level set method and the one from Theorem 4.1 match quite well. Especially, before singularity, the result from level set method are very accurate, which is shown in Table 6. At time 0.101333 the errors in  $\bar{\rho}$ ,  $\bar{J}$  and  $\bar{E}$  are of order  $10^{-2}$ ,  $10^{-4}$  and  $10^{-4}$  respectively with step size  $\Delta x = 0.02$  and  $\Delta p = 0.02$ . After singularity we still get very good resolution as in Figs. 5 and 6. we still use periodic and constant boundary conditions in the case of solving for velocity and  $f$ , respectively. For the integration support size  $\epsilon$ , as in Example 1, we also notice that before singularity,  $\epsilon$  should be larger and after singularity smaller  $\epsilon$  is preferred. The  $\min_{|\phi| \leq 0.01} |\phi_p|$  at time about 0.1, 0.4 and 0.8 are 0.681421, 0.170917 and 0.167495 respectively. This confirms that optimal support size  $\epsilon$  gets smaller when  $\min_{|\phi| \leq \epsilon'} |\phi_p|$  gets smaller.

### 6.2 Wave Equation

In this section, we test the following Hamiltonian

$$H(x, p) = c(x)|p|, \quad H_p = c(x) \frac{p}{|p|}.$$

This Hamiltonian comes from the WKB expansion of wave equation (1.6).

**Table 6** Example 2, table of  $L^1$  error for each density momentum and energy at different time and support size  $\epsilon = mh$ ,  $m = 2, 3, 4, 5, 6$  with step size  $[0.02, 0, 02]$ 1. Error for averaged density  $\bar{\rho}$ 

$t$	$\epsilon = 2h$	$\epsilon = 3h$	$\epsilon = 4h$	$\epsilon = 5h$	$\epsilon = 6h$
0.101333	0.0201441257	0.0173173587	0.0163551543	0.0162149049	0.0160895224
0.405333	0.1353771931	0.2096008463	0.2570685836	0.2899839171	0.3458325428
0.810667	0.3638322043	0.3349340467	0.3721443546	0.4093349941	0.4441836011

2. Error for averaged momentum  $\bar{J}$ 

$t$	$\epsilon = 2h$	$\epsilon = 3h$	$\epsilon = 4h$	$\epsilon = 5h$	$\epsilon = 6h$
0.101333	0.0024015908	0.0008418077	0.0004557995	0.0005120796	0.0006508837
0.405333	0.0824243578	0.1045426391	0.1040800957	0.1170525606	0.1358341234
0.810667	0.2234771392	0.2049319728	0.2283069834	0.2550550387	0.2760111370

3. Error for averaged energy  $\bar{E}$ 

$t$	$\epsilon = 2h$	$\epsilon = 3h$	$\epsilon = 4h$	$\epsilon = 5h$	$\epsilon = 6h$
0.101333	0.0010576917	0.0005229522	0.0006651123	0.0009172565	0.0012734635
0.405333	0.0318257465	0.0377931322	0.0354224554	0.0465411020	0.0560490059
0.810667	0.0973139057	0.0965972571	0.1084100663	0.1206675156	0.1305867870

**Table 7** Example 3, table of  $L^1$  error for each density momentum and energy at different time and support size  $\epsilon = mh$ ,  $m = 2, 3, 4, 5, 6$  with step size  $[0.02, 0.02]$ 1. Error for averaged density  $\bar{\rho}$ 

$t$	$\epsilon = 2h$	$\epsilon = 3h$	$\epsilon = 4h$	$\epsilon = 5h$	$\epsilon = 6h$
0.351500	0.1243459867	0.1243459894	0.1243460235	0.1243461163	0.1243450280
0.408500	0.1269397689	0.1269397703	0.1269398218	0.1269404161	0.1269415934
1.007000	0.1667407901	0.1667406964	0.1667402289	0.1667377286	0.1667242841

2. Error for averaged momentum  $\bar{J}$ 

$t$	$\epsilon = 2h$	$\epsilon = 3h$	$\epsilon = 4h$	$\epsilon = 5h$	$\epsilon = 6h$
0.351500	0.1122599833	0.1122599806	0.1122599464	0.1122595708	0.1122560508
0.408500	0.1260541833	0.1260541819	0.1260541304	0.1260535361	0.1260514986
1.007000	0.1667388478	0.1667387542	0.1667382866	0.1667357863	0.1667223418

3. Error for averaged energy  $\bar{E}$ 

$t$	$\epsilon = 2h$	$\epsilon = 3h$	$\epsilon = 4h$	$\epsilon = 5h$	$\epsilon = 6h$
0.351500	0.0319705467	0.0319439985	0.0319378147	0.0319350105	0.0319335234
0.408500	0.0321329464	0.0321274079	0.0321255184	0.0321246575	0.0321242228
1.007000	0.0428831029	0.0428384220	0.0428303218	0.0428281333	0.0428269787

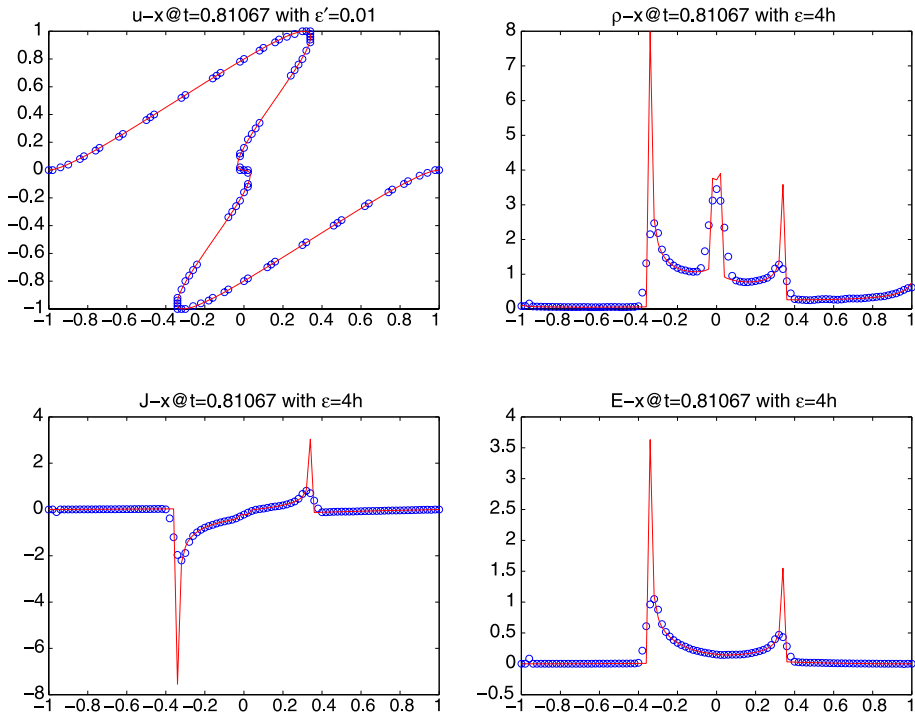


**Fig. 6** Example 2, at  $t = 0.810667$ . Sub-figures, from up left, are velocity, density, momentum and energy with  $\epsilon' = 0.01$  and  $\epsilon = 4h$ . Circles and solid lines represent the results from integration and superposition, respectively

Now we are still interested in the following quantities

$$\bar{\rho} = \int f \delta(\Phi) dp,$$

$$\bar{J} = \int c(x) \frac{p}{|p|} f \delta(\Phi) dp,$$

$$\bar{E} = \int c(x) |p| f \delta(\Phi) dp.$$

We call the last two quantities momentum and energy. We now test them by the following examples from [15].

*Example 3* 1D and constant speed  $c(x) = 1$ .

$$S_0 = -\frac{x^2 - 0.25}{4}, \tag{6.2}$$

$$A_0 = I_{[-0.7, -0.3] \cup [0.3, 0.7]}(x), \tag{6.3}$$

where  $\rho_0 = A_0^2/c^2$ . Here  $I(\Omega)$  is the characteristic function of  $\Omega$ .

**Table 8** Example 3, table of  $L^1$  error for each density momentum and energy at different time and support size  $\epsilon = mh$ ,  $m = 2, 3, 4, 5, 6$  with step size  $[0.01, 0.01]$

1. Error for averaged density  $\bar{\rho}$

$t$	$\epsilon = 2h$	$\epsilon = 3h$	$\epsilon = 4h$	$\epsilon = 5h$	$\epsilon = 6h$
0.351500	0.0730752707	0.0730752707	0.0730752707	0.0730752707	0.0730752707
0.403750	0.0688340482	0.0688340482	0.0688340482	0.0688340482	0.0688340482
1.002250	0.0851973109	0.0851973109	0.0851973109	0.0851973109	0.0851973109

2. Error for averaged momentum  $\bar{J}$

$t$	$\epsilon = 2h$	$\epsilon = 3h$	$\epsilon = 4h$	$\epsilon = 5h$	$\epsilon = 6h$
0.351500	0.0181718495	0.0181535625	0.0181474769	0.0181448518	0.0181435050
0.403750	0.0171266513	0.0171167153	0.0171139650	0.0171129193	0.0171125731
1.002250	0.0217289289	0.0216981950	0.0216887067	0.0216847314	0.0216827964

3. Error for averaged energy  $\bar{E}$

$t$	$\epsilon = 2h$	$\epsilon = 3h$	$\epsilon = 4h$	$\epsilon = 5h$	$\epsilon = 6h$
0.351500	0.0027198709	0.0027231238	0.0027322929	0.0027457254	0.0027629154
0.403750	0.0024778875	0.0024666502	0.0024692810	0.0024739515	0.0024868737
1.002250	0.0031984964	0.0031922123	0.0031985274	0.0032105926	0.0032280559

In this case, we solve the level set equation (2.3) with  $H = c|p|$ . Since  $\nabla_p H = c \frac{p}{|p|}$ , undefined at  $p = 0$ , as in [15] we choose to exclude this singular set in our computation domain. In simulation, we exclude the set

$$\Omega_{exclude} = \left\{ (x, p) \mid |p| < \max_i \Delta p_i, i = 1, 2, \dots, n \right\},$$

where  $\Delta p_i$  is the step size in  $p_i$  direction. The multi-valued density is computed by (3.6). In this example, the initial velocity is  $u_0 = -x/2$ , which is decreasing. We know that the solution will become multi-valued immediately since the wave with negative speed is on the right and moves towards left, while the wave with positive speed is on the left and moves towards right.

In the simulation, the mesh size is picked as  $[0.02, 0.02]$ . In this example, the multi-valued density is computed by (3.6). Constant boundary condition is used in this case. From Figs. 7, 8 and 9, we see that those average quantities match nicely, which numerically shows the superposition. Meanwhile the Table 7 of error gives the numerical  $L^1$  error of density, momentum and energy at different time and support  $\epsilon$ . We notice that the error doesn't depend on the support size  $\epsilon$ . Thus we refined our mesh size to be  $[0.01, 0.01]$  and show the  $L^1$  error in Table 8. We could easily see that the error doesn't change with respect to  $\epsilon$ . Moreover, a table of  $\phi_p$  is also listed here in Table 9. We notice that all  $\min_{|\phi| \leq 0.01} |\phi_p|$ 's are 1. Thus the error is independent of optimal support size  $\epsilon$ , which is observed in the Tables 7 and 8.

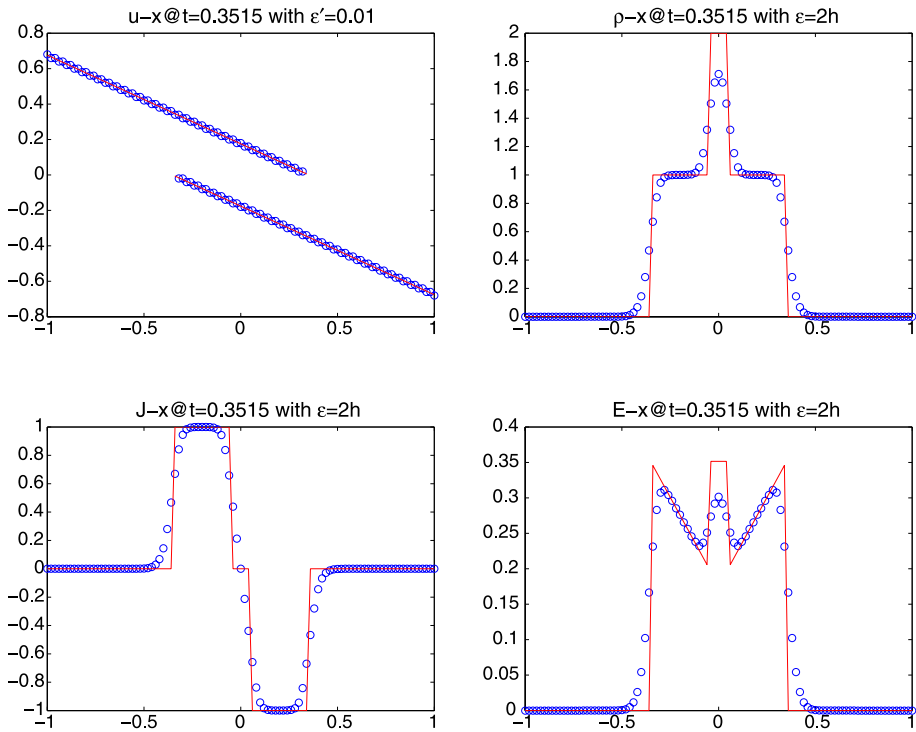


**Fig. 7** Example 3, at  $t = 0.3515$ . Sub-figures, from *up left*, are velocity,  $g = 1$ ,  $g = \nabla_p H$  and  $g = H$  with  $\epsilon' = 0.01$  and  $\epsilon = 2h$ . Circles and solid lines represent the results from integration and superposition, respectively

**Table 9** Example 3, table of  $\max_{|\phi| \leq 0.01} |\phi_p|$  at different times and mesh sizes

$[\Delta x, \Delta p]$	Time $\approx 0.35$	Time $\approx 0.4$	Time $\approx 1$
[0.02, 0.02]	1.000000	1.000000	1.000000
[0.01, 0.01]	1.000000	1.000000	1.000000

*Example 4 1D and variable speed  $c(x)$*

$$S_0 = -\frac{x^2}{4}, \tag{6.4}$$

$$A_0 = I_{[-0.45, -0.25] \cup [0.25, 0.45]}(x), \tag{6.5}$$

with  $c(x) = 3 + 1.5 \tanh(x)$  and  $\rho_0 = A_0^2/c^2$ .

A similar example was used in [15]. Here, the example taken is a re-scaled one for the save of computation time. Constant boundary condition is used in this case. See the results in Figs. 10, 11 and 12. Here, instead of (3.6), the multi-valued density is computed by (3.4)

$$\rho_i \in \left\{ \frac{f}{|\det(\nabla_p \Phi)|} \mid \Phi(t, x, p) = 0 \right\}.$$

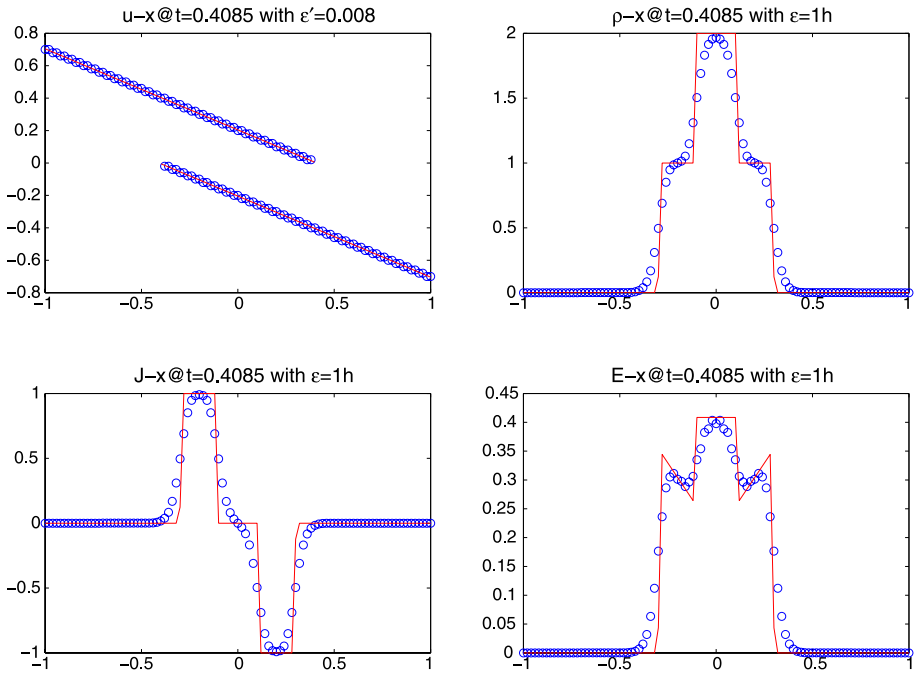


**Fig. 8** Example 3, at  $t = 0.408500$ . Sub-figures, from *up left*, are velocity,  $g = 1$ ,  $g = \nabla_p H$  and  $g = H$  with  $\epsilon' = 0.008$  and  $\epsilon = h$ . Circles and solid lines represent the results from integration and superposition, respectively

**Table 10** Example 4, table of  $L^1$  error for each density momentum and energy at different time and support size  $\epsilon = mh$ ,  $m = 2, 3, 4, 5, 6$

1. Error for averaged density  $\bar{\rho}$

$t$	$\epsilon = 2h$	$\epsilon = 3h$	$\epsilon = 4h$	$\epsilon = 5h$	$\epsilon = 6h$
0.050510	0.0004124339	0.0002574400	0.0002064428	0.0001860470	0.0001836040
0.151460	0.0066038938	0.0065472959	0.0065354958	0.0065220750	0.0065486092
0.252433	0.0005593891	0.0002781005	0.0002250622	0.0002342965	0.0003174496

2. Error for averaged momentum  $\bar{J}$

$t$	$\epsilon = 2h$	$\epsilon = 3h$	$\epsilon = 4h$	$\epsilon = 5h$	$\epsilon = 6h$
0.050510	0.1314190720	0.1314198912	0.1314201536	0.1314201914	0.1314201904
0.151460	0.1070391216	0.1070397427	0.1070394493	0.1070387782	0.1070392338
0.252433	0.1516576004	0.1516669850	0.1516688414	0.1516792368	0.1516929572

3. Error for averaged energy  $\bar{E}$

$t$	$\epsilon = 2h$	$\epsilon = 3h$	$\epsilon = 4h$	$\epsilon = 5h$	$\epsilon = 6h$
0.050510	0.0237754984	0.0237694404	0.0237608625	0.0237498011	0.0237362724
0.151460	0.0292403331	0.0292340795	0.0292253946	0.0292141528	0.0292005134
0.252433	0.0249560424	0.0249503050	0.0249415895	0.0249318013	0.0249203468

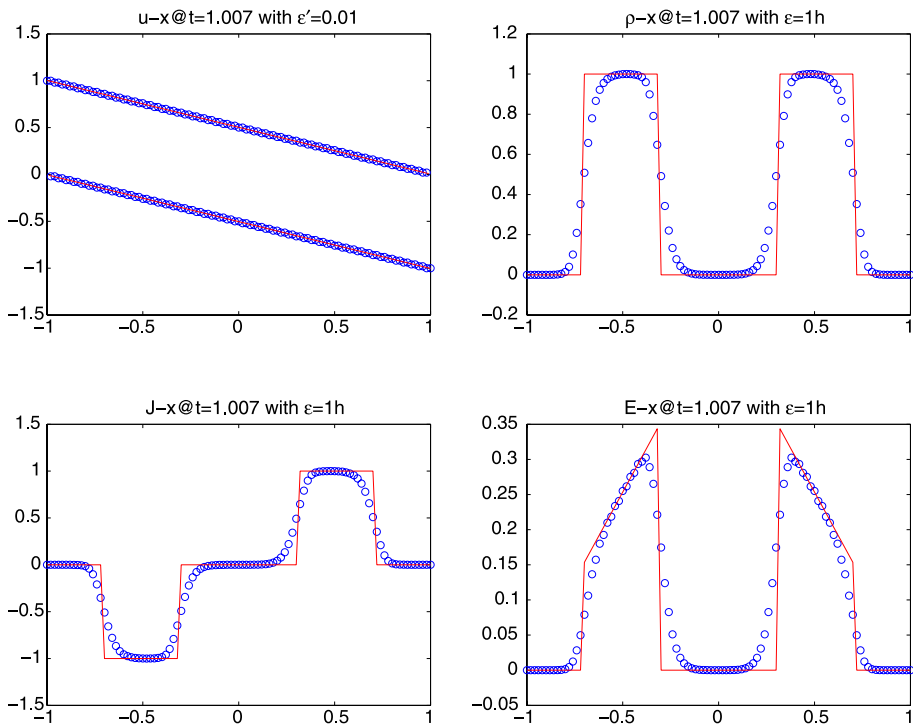


**Fig. 9** Example 3, at  $t = 1.00700$ . Sub-figures, from *up left*, are velocity,  $g = 1$ ,  $g = \nabla_p H$  and  $g = H$  with  $\epsilon' = 0.01$  and  $\epsilon = h$ . Circles and solid lines represent the results from integration and superposition, respectively

Central difference is used to approximate the Jacobian  $\nabla_p \Phi$ . Then the multi-valued data  $\{\tilde{\rho}(t, x_j, u_i), j = 1, \dots, M, i = 1, \dots, N\}$  could be found. Note that those points  $\{x_j, j = 1, \dots, M\}$  might not be the same as our grid points from partition of  $x$ . Thus, a simple linear interpolation is also used to compute the  $\rho(t, x)$  at any grid point  $x$ .

From Figs. 10, 11 and 12, we can clearly see the waves crossing and changing its velocity since  $c$  is not a constant. Moreover, the error Table 10 shows the  $L^1$  error of the results from integration and superposition. The  $\min_{|\phi| \leq 0.01} |\phi_p|$ 's at time about 0.05, 0.15 and 0.25 are 0.927167, 0.799815 and 0.696568 respectively with optimal support  $\epsilon$ 's are  $6h$ ,  $5h$  and  $4h$  respectively in Table 10.

*Remark 1* In this Example 4, numerical error is also introduced by the approximation of  $|\det(\nabla_p \Phi)|$ . Especially, when  $u_i$  coincides with any of computational grids,  $|\det(\nabla_p \Phi)| = 0$  and  $\rho_i = \infty$  at those points. This could result in huge numerical error. Numerical tests are performed on this issue in two dimensional space, and large error is observed. Thus a new approximation of  $|\det(\nabla_p \Phi)|$  is expected in order to use (3.4).

*Remark 2* From above examples, we notice that the integration support  $\epsilon$  in (5.2) plays an important role in the error control. We find out that the dependence of  $\epsilon$  on  $\phi_p$  can be characterized by a global (in  $x$ ) indicator

$$Ind(\phi) := \min_{|\phi| \leq \epsilon'} |\phi_p|.$$

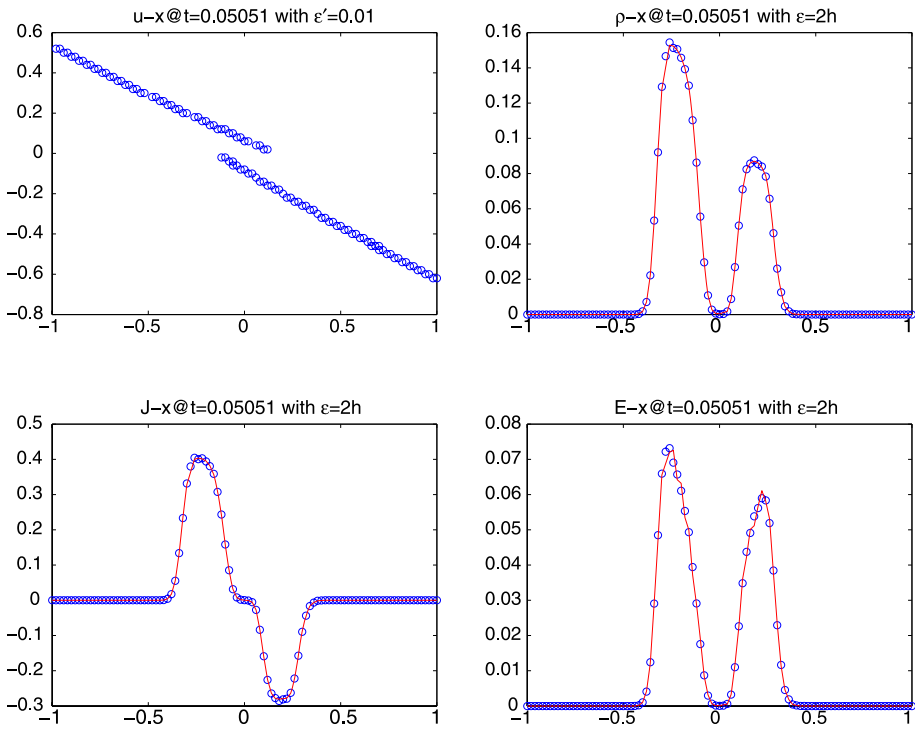


**Fig. 10** Example 4, at  $t = 0.05051$ . Sub-figures, from *up left*, are velocity,  $g = 1$ ,  $g = \nabla_p H$  and  $g = H$  with  $\epsilon' = 0.01$  and  $\epsilon = 2h$ . Circles and solid lines represent the results from integration and superposition, respectively

The smaller  $Ind(\phi)$  is, the smaller  $\epsilon$  is.

Meanwhile, since at the turning points  $\phi_p = 0$ , optimal  $\epsilon$  should get smaller after turning points appears after singularity.

**Acknowledgements** This research was supported by the National Science Foundation under Grant DMS05-05975.

**Appendix**

Here we justify the formula (3.6)

$$\rho(t, x(t, \alpha)) = \frac{\rho_0(\alpha)}{|\det(\Gamma)|}, \tag{A.1}$$

where  $x = x(t, \alpha)$  is the characteristics satisfying  $\frac{dx}{dt} = \nabla_p H|_{p=\nabla_x S}$ , and  $\Gamma = \frac{\partial x(t, \alpha)}{\partial \alpha}$ . Let  $J = \det\left(\frac{\partial x}{\partial \alpha}\right)$ , then

$$\frac{\partial}{\partial t} J = \frac{\partial}{\partial t} \det\left(\frac{\partial x_i}{\partial \alpha_j}(t, \alpha)\right) = \sum_{i,j} A_i^j \frac{\partial}{\partial t} \frac{\partial x_i}{\partial \alpha_j}(t, \alpha),$$

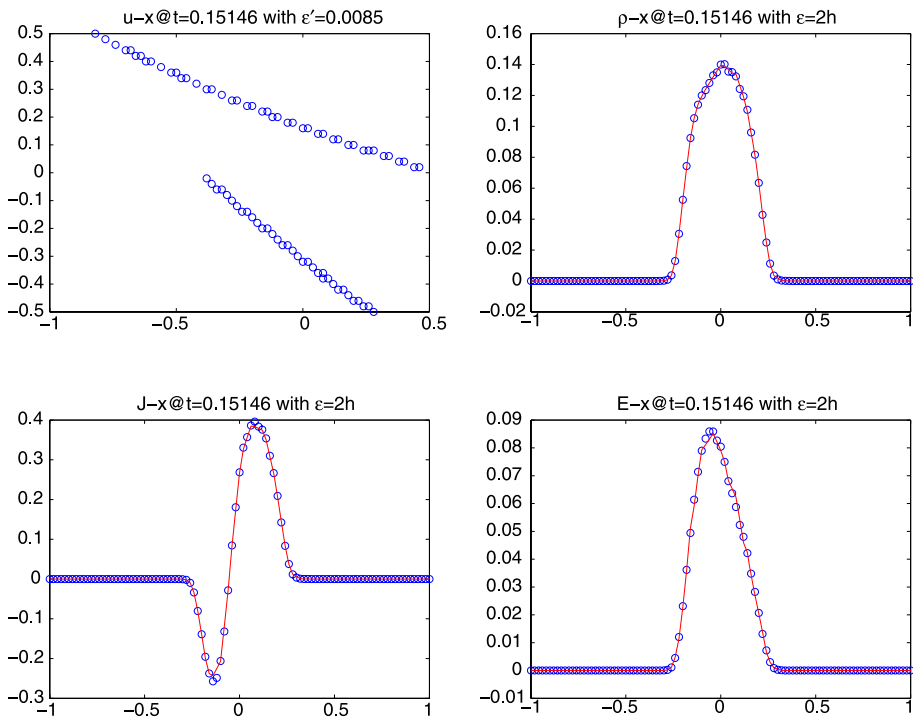


**Fig. 11** Example 4, at  $t = 0.15146$ . Sub-figures, from up left, are velocity,  $g = 1$ ,  $g = \nabla_p H$  and  $g = H$  with  $\epsilon' = 0.0085$  and  $\epsilon = 2h$ . Circles and solid lines represent the results from integration and superposition, respectively

where  $A_i^j$  is the minor of the element  $\frac{\partial x_i}{\partial \alpha_j}$  of the matrix  $\frac{\partial x}{\partial \alpha}$ .

The minor satisfies

$$\sum_j \frac{\partial x_k}{\partial \alpha_j} A_i^j = \delta_i^k J, \quad \delta_i^k = \begin{cases} 1, & k = i, \\ 0, & k \neq i. \end{cases}$$

Thus the use of the equation  $\frac{dx}{dt} = \nabla_p H$  gives

$$\begin{aligned} \frac{\partial J}{\partial t} &= \sum_{i,j} A_i^j \frac{\partial}{\partial \alpha_j} \frac{\partial}{\partial t} x_i = \sum_{i,j} A_i^j \frac{\partial}{\partial \alpha_j} (\partial_{p_i} H) \\ &= \sum_{i,j,k} A_i^j \frac{\partial x_k}{\partial \alpha_j} \left( \frac{\partial}{\partial x_k} (\partial_{p_i} H) \right) = \sum_i \frac{\partial}{\partial x_i} (\partial_{p_i} H) J \\ &= \nabla_x \cdot (\nabla_p H) J. \end{aligned}$$

For any domain  $\Omega$ , the change of variables  $\alpha \rightarrow x(t, \alpha)$  leads to

$$\int_{x(t,\Omega)} \rho(t, x) dx = \int_{\Omega} \rho(t, x(t, \alpha)) J d\alpha,$$

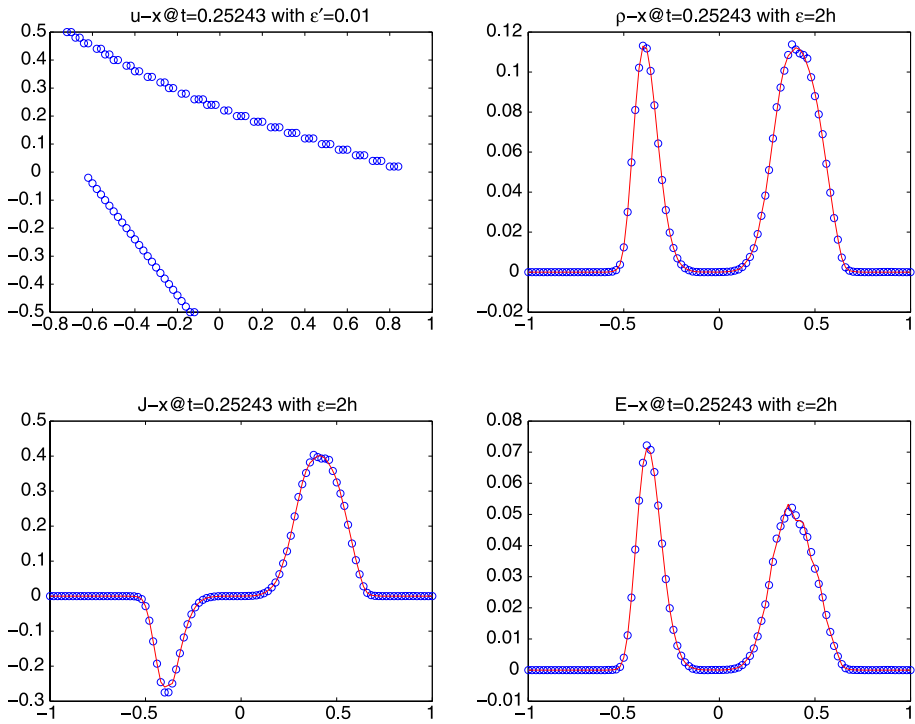


**Fig. 12** Example 4, at  $t = 0.25243$ . Sub-figures, from *up left*, are velocity,  $g = 1$ ,  $g = \nabla_p H$  and  $g = H$  with  $\epsilon' = 0.01$  and  $\epsilon = 2h$ . Circles and solid lines represent the results from integration and superposition, respectively

This, by differentiation in  $t$ , gives

$$\begin{aligned}
 \frac{d}{dt} \int_{x(t,\Omega)} \rho(t, x) dx &= \int_{\Omega} \left( \rho_t + \frac{dx}{dt} \cdot \nabla_x \rho \right) J + \rho \frac{\partial J}{\partial t} d\alpha \\
 &= \int_{\Omega} (\rho_t + H_p \cdot \nabla_x \rho) J + \rho \nabla_x \cdot \nabla_p H J d\alpha \\
 &= \int_{\Omega} [\rho_t + \nabla_x \cdot (\rho \nabla_p H)] J d\alpha \\
 &= \int_{x(t,\Omega)} (\rho_t + \nabla_x \cdot (\rho \nabla_p H)) dx \\
 &= 0.
 \end{aligned}$$

Therefore, we obtain

$$\int_{x(t,\Omega)} \rho(t, x) dx = \int_{\Omega} \rho_0(\alpha) d\alpha.$$

Since this holds for any  $\Omega$ , we must have

$$\rho(t, x(t, \alpha)) J = \rho_0(\alpha),$$

which gives (A.1), except for the absolute sign on  $J$ , which is needed to ensure positivity of the density after singularity.

## References

1. Beyer, R.P., LeVeque, R.J.: Analysis of a one-dimensional model for the immersed boundary method. *SIAM J. Numer. Anal.* **29**(2), 332–364 (1992)
2. Brenier, Y., Corrias, L.: A kinetic formulation for multi-branch entropy solutions of scalar conservation laws. *Ann. Inst. Henri Poincaré Anal. Non Linéaire* **15**(2), 169–190 (1998)
3. Cheng, L.-T.: An Efficient level set method for constructing wave fronts in three space dimensions. *UCLA CAM Report* (15) (2006)
4. Cheng, L.-T., Liu, H., Osher, S.: Computational high-frequency wave propagation using the level set method, with applications to the semi-classical limit of Schrödinger equations. *Commun. Math. Sci.* **1**(3), 593–621 (2003)
5. Crandall, M.G., Lions, P.-L.: Viscosity solutions of Hamilton-Jacobi equations. *Trans. Am. Math. Soc.* **277**(1), 1–42 (1983)
6. Engquist, B., Runborg, O.: Multi-phase computations in geometrical optics. *J. Comput. Appl. Math.* **74**(1–2), 175–192 (1996). *TICAM Symposium* (Austin, TX, 1995)
7. Engquist, B., Runborg, O.: Computational high frequency wave propagation. In: *Acta Numerica*, vol. 12, pp. 181–266. Cambridge University Press, Cambridge (2003)
8. Engquist, B., Tornberg, A.-K., Tsai, R.: Discretization of Dirac delta functions in level set methods. *J. Comput. Phys.* **207**(1), 28–51 (2005)
9. Gosse, L.: Using  $K$ -branch entropy solutions for multivalued geometric optics computations. *J. Comput. Phys.* **180**(1), 155–182 (2002)
10. Gosse, L., Jin, S., Li, X.: Two moment systems for computing multiphase semiclassical limits of the Schrödinger equation. *Math. Models Methods Appl. Sci.* **13**(12), 1689–1723 (2003)
11. Gottlieb, S., Shu, C.-W., Tadmor, E.: Strong stability-preserving high-order time discretization methods. *SIAM Rev.* **43**(1), 89–112 (2001) (electronic)
12. Harten, A.: Preliminary results on the extension of ENO schemes to two-dimensional problems. In: *Non-linear Hyperbolic Problems*, (St. Etienne, 1986). *Lect. Notes in Math.*, vol. 1270, pp. 23–40. Springer, Berlin (1987)
13. Harten, A.: ENO schemes with subcell resolution. *J. Comput. Phys.* **83**(1), 148–184 (1989)
14. Jin, S., Li, X.: Multi-phase computations of the semiclassical limit of the Schrödinger equation and related problems: Whitham vs. Wigner. *Physica D* **182**(1–2), 46–85 (2003)
15. Jin, S., Liu, H., Osher, S., Tsai, R.: Computing multi-valued physical observables for the high frequency limit of symmetric hyperbolic systems. *J. Comput. Phys.* **210**(2), 497–518 (2005)
16. Jin, S., Liu, H., Osher, S., Tsai, Y.-H.R.: Computing multivalued physical observables for the semiclassical limit of the Schrödinger equation. *J. Comput. Phys.* **205**(1), 222–241 (2005)
17. Jin, S., Osher, S.: A level set method for the computation of multivalued solutions to quasi-linear hyperbolic PDEs and Hamilton-Jacobi equations. *Commun. Math. Sci.* **1**(3), 575–591 (2003)
18. Kružkov, S.N.: First order quasilinear equations with several independent variables. *Mat. Sb. (N.S.)* **81**(123), 228–255 (1970)
19. Liu, H., Cheng, L.-T., Osher, S.: A level set framework for capturing multi-valued solutions to nonlinear first-order equations. *J. Sci. Comput.* **29**(3), 353–373 (2006)
20. Liu, H., Osher, S., Tsai, R.: Multi-valued solution and level set methods in computational high frequency wave propagation. *Commun. Comput. Phys.* **1**(5), 765–804 (2006)
21. Liu, H., Wang, Z.: Computing multi-valued velocity and electric fields for 1d Euler-Poisson equations. *Appl. Numer. Math.* **57**(5–7), 821–836 (2007)
22. Liu, H., Wang, Z.: A filed-space based level set method for computing multi-valued solutions to 1d Euler-Poisson equations. *J. Comput. Phys.* **225**(1), 591–614 (2007)
23. Min, C.: Local level set method in high dimension and codimension. *J. Comput. Phys.* **200**(1), 368–382 (2004)
24. Osher, S., Cheng, L.-T., Kang, M., Shim, H., Tsai, Y.-H.: Geometric optics in a phase-space-based level set and Eulerian framework. *J. Comput. Phys.* **179**(2), 622–648 (2002)
25. Osher, S., Shu, C.-W.: High-order essentially nonoscillatory schemes for Hamilton-Jacobi equations. *SIAM J. Numer. Anal.* **28**(4), 907–922 (1991)
26. Peng, D., Merriman, B., Osher, S., Zhao, H., Kang, M.: A PDE-based fast local level set method. *J. Comput. Phys.* **155**(2), 410–438 (1999)

27. Raviart, P.-A.: On the numerical analysis of particle simulations in plasma physics. In: *Nonlinear Partial Differential Equations and Their Applications*. Collège de France Seminar, vol. IV, Paris, 1981/1982. Res. Notes in Math., vol. 84, pp. 173–193. Pitman, Boston (1983)
28. Shu, C.-W.: High order ENO and WENO schemes for computational fluid dynamics. In: *High-Order Methods for Computational Physics*. Lect. Notes Comput. Sci. Eng., vol. 9, pp. 439–582. Springer, Berlin (1999)
29. Shu, C.-W., Osher, S.: Efficient implementation of essentially nonoscillatory shock-capturing schemes. *J. Comput. Phys.* **77**(2), 439–471 (1988)
30. Shu, C.-W., Osher, S.: Efficient implementation of essentially nonoscillatory shock-capturing schemes. II. *J. Comput. Phys.* **83**(1), 32–78 (1989)
31. Towers, J.: Two methods for discretizing a delta function supported on a level set. *J. Comput. Phys.* **220**(2), 915–931 (2007)
32. Whitham, G.B.: *Linear and Nonlinear Waves*. Wiley, New York (1974). Pure Appl. Math.